phys. stat. sol. (a) **201**, No. 1, 26–45 (2004) / **DOI** 10.1002/pssa.200306715

# Plastic deformation of yttria stabilized cubic zirconia single crystals I. Activation parameters of deformation

**A. Tikhonovsky, M. Bartsch,** and **U. Messerschmidt***

Max-Planck-Institut für Mikrostrukturphysik, Weinberg 2, 06120 Halle/Saale, Germany

Received 19 June 2003, revised 30 September 2003, accepted 17 October 2003
Published online 4 December 2003

**PACS** 61.72.Ff, 62.20.Fe, 81.05.Je, 81.40.Cd, 81.40.Lm, 81.70.Bt

Cubic zirconia containing 10 mol% yttria was deformed along the hard ⟨100⟩ direction and materials with 15 and 20 mol% yttria along the soft ⟨112⟩ orientation between 1400 °C and the lowest possible temperatures without brittle failure. The 10% material shows along ⟨100⟩ a strong increase in the flow stress at decreasing temperature, while the materials with 15 and 20 mol% yttria along ⟨112⟩ exhibit a higher flow stress with a weak temperature dependence. The activation parameters of deformation were measured by stress relaxation and temperature change tests. The microstructures are studied by high-voltage transmission electron microscopy. The results are interpreted by long-range interactions between the dislocations, the Peierls mechanism at the lowest temperatures, precipitation hardening between 500 °C and 800 °C, and by recovery-controlled deformation at high temperatures. The occurrence of plastic instabilities are described in Part II [phys. stat. sol. (a) **201**, No. 1 (2004)] of this paper.



## 1 Introduction

Above about 2400 °C, pure zirconia has the cubic fluorite structure. Below that temperature, it transforms to a tetragonal phase and finally below about 1200 °C to a monoclinic one. However, the cubic high-temperature phase can be stabilized to lower temperatures by adding aliovalent cations. The most intensively studied system is the zirconia-yttria ($ZrO_2$–$Y_2O_3$) system. Addition of more than about 8 mol% yttria stabilizes the cubic phase ($c$-$ZrO_2$) down to room temperature. It should be the matrix phase of two-phase materials containing precipitates of the tetragonal phase. These materials show a remarkable high-temperature strength owing to an effective precipitation hardening mechanism [1]. Studies of the plastic deformation of the cubic phase are a prerequisite of understanding the mechanical properties of these more complex zirconia materials. Besides, cubic zirconia with higher yttria concentrations may also be a promising component to other high-temperature materials owing to its high flow stress at high temperatures (about 300 MPa at 1400 °C [2]).

Plastic deformation of cubic zirconia single crystals at high temperatures has extensively been studied by the groups of A. H. Heuer and A. Dominguez-Rodriguez [2–10]. Crystals with 9.4 mol% yttria were mostly deformed at 1400 °C along the soft ⟨112⟩ compression axis to promote single slip on the easy {001}1/2⟨110⟩ slip system [2–4]. The temperature dependence of the flow stress was first investigated between 1200 and 1500 °C [5] and later on in creep up to 1800 °C (e.g. [9]). Slip on non-cube planes was first studied in Ref. [6]. Addition of more than about 9 mol% yttria up to about 20 mol% leads to an increase in the flow stress [7, 9, 10]. The results around 1400 °C were first explained by solution hardening controlling the dislocation mobility (e.g. [5]). Later on, it was argued that the deformation at 1400 °C

* Corresponding author: e-mail: um@mpi-halle.de, Phone: +49 345 5582 927, Fax: +49 345 5511223

is controlled by recovery processes of the dislocation structure [11] where the recovery rate depends on the cationic diffusion coefficient which, in turn, depends on the yttrium concentration [12]. This view was elaborated in [13] and discussed on the basis of a creep model by Burton (e.g. [14]) with a transition from climb-recovery controlled deformation above about 1500 °C to viscous glide, controlled by point defect atmospheres around the dislocations below that temperature [8, 9]. This mechanism was also claimed in a creep study at low strain rates [15]. Thus, the high-temperature deformation of *c*-$ZrO_2$ is experimentally well documented though the interpretation is not as clear.

So far, *c*-$ZrO_2$ had been supposed to be brittle below about 1000 °C. However, by using a low strain rate and by careful specimen preparation, *c*-$ZrO_2$ with about 10 mol% $Y_2O_3$ can be deformed plastically in the soft ⟨112⟩ orientation down to 400 °C [16, 17] and under confining hydrostatic pressure even down to 250 °C [18]. In addition to the high-temperature range discussed above, the material shows three temperature ranges with clearly different deformation mechanisms, an athermal range around 1150 °C, a range where localized obstacles control the dislocation mobility below about 1000 °C and a range below about 500 °C where the Peierls mechanism is superimposed [17, 19]. The state of the understanding of the deformation mechanisms of *c*-$ZrO_2$ has been reviewed in Refs. [20, 21].

However, the data available on the low-temperature deformation of *c*-$ZrO_2$, i.e. below about 1200 °C, are restricted to $ZrO_2$-10 mol% $Y_2O_3$ and, except a few experiments near 1150 °C [13], to the soft ⟨112⟩ orientation. It is the aim of the present study to supplement these data by:

(1) Plastic deformation experiments on $ZrO_2$-10mol%$Y_2O_3$ in the hard ⟨100⟩ orientation, where the easy {001}1/2⟨110⟩ slip system has a zero orientation factor, in order to activate slip on the {110} or {111} planes. Previous studies by macroscopic deformation [6] and by high-temperature *in situ* straining experiments in a high-voltage electron microscope (HVEM) [22] have shown that on these planes slip is controlled by processes different from those on the easy {001} planes.

(2) Experiments on *c*-$ZrO_2$ with 15 and 20 mol% $Y_2O_3$ to study the influence of the stabilizer concentration on the plastic properties.

All experiments were performed between 1400 °C down to the lowest temperatures where plastic deformation could be achieved to better characterize the low-temperature mechanisms. For some deformation conditions, the dislocation microstructure was studied by conventional transmission electron microscopy in the HVEM. The basic deformation data are described in Part I of this paper. Part II presents the results on plastic instabilities, which occur in the materials with higher yttria concentrations, as observed before [10].

## 2 Experimental

Rectangular bars of fully stabilized zirconia single crystals about $8 \times 2 \times 2$ mm$^3$ in size were cut and carefully polished from large pieces[**] with 10, 15 and 20 mol% yttria. The long axis was oriented for compression along [100] with (010) and (001) side faces for the material with 10 mol% $Y_2O_3$ and along $[1\bar{1}2]$ with $(\bar{1}11)$ and (110) side faces for the materials with 15 and 20 mol% $Y_2O_3$. The crystals were deformed in a single screw testing machine, usually at a constant strain rate of $\dot{\varepsilon} = 10^{-5}$ s$^{-1}$. Further experimental details are described, e.g., in Refs. [13, 16].

To study the activation parameters of the plastic deformation, stress relaxation tests were performed. The strain rate sensitivity $r$ of the flow stress $\sigma$ (engineering stress) was calculated from the inverse slope of the relaxation curves plotted as $\ln(-\dot{\sigma})$ versus $\sigma$

$$r = \mathrm{d}\sigma/\mathrm{d}\ln\dot{\varepsilon} = \mathrm{d}\sigma/\mathrm{d}\ln(-\dot{\sigma}) . \quad (1)$$

Usually, the strain rate sensitivity was determined at the beginning of the relaxation tests so that it corresponds to the strain rate during deformation just before the relaxation tests started. Frequently, a second relaxation followed the original one at a stress slightly below the starting stress of the original relaxation so that the plastic strain between both relaxations is very small. The differences between the original

[**] Former Ceres Corp., Waltham MA

relaxation tests and these "repeated" relaxations, taken before a steady state microstructure is reached again, give information on structural changes during the first relaxations. A few strain rate cycling experiments were carried out for comparison with the results of the relaxation tests.

In order to determine the activation energy of the plastic deformation, temperature change tests were performed. The specimens were partially unloaded before changing the temperature. The deformation was resumed at the new temperature after thermal equilibrium was reached. Frequently, a yield drop effect occurred after the temperature change owing to changes in the microstructure. For calculating the temperature sensitivity $\Delta\sigma/\Delta T$, the stress strain curve after the lower yield point was back-extrapolated linearly to the strain of the temperature change. Thus, the temperature sensitivity corresponds to the differences in the steady state deformation behaviour. The activation enthalpy was calculated according to

$$\Delta H = -kT^2(\Delta\sigma/\Delta T)_{\dot{\varepsilon}}/r\ . \tag{2}$$

$T$ is the average temperature $T = (T_1T_2)^{1/2}$ and $r$ the average value of the strain rate sensitivities measured from relaxations immediately before and after the temperature change $r = (r_1 + r_2)/2$.

The structure of the slip bands in the deformed specimens was investigated by optical stress birefringence and reflection microscopy. Specimens for transmission electron microscopy were cut either parallel to the side faces or to the cross section. They were investigated in the HVEM under diffraction contrast conditions.

## 3 Results

### 3.1 Macroscopic deformation tests

The first part of this section describes the results of the tests on $ZrO_2$-10 mol% $Y_2O_3$ deformed in compression along the hard ⟨100⟩ orientation at a strain rate of $10^{-5}$ $s^{-1}$. Figure 1 shows selected stress-strain curves taken at different temperatures. Below 500 °C, the specimens broke without remarkable plastic deformation. Particularly at low temperatures, the deformation curves show a strong yield drop effect. The strain hardening coefficient is always low. It is slightly negative at high and low temperatures and slightly positive at intermediate ones. During almost steady state deformation, the stress-strain curves were interrupted by stress relaxation, strain rate change and temperature change tests. The critical flow stress $\sigma_y$ is obtained either from the upper yield points or, for curves without a yield drop effect, from a back-extrapolation of the steady state flow range onto the elastic line. $\sigma_y$ is plotted in Fig. 2 as a function of temperature. The temperature dependence of the flow stress in the ⟨100⟩ orientation can be compared with reference data in the soft ⟨112⟩ orientation at $10^{-6}$ $s^{-1}$, determined before [16, 17]. The flow stresses along ⟨112⟩ are always lower than those along ⟨100⟩ except at the highest temperature of 1400 °C.

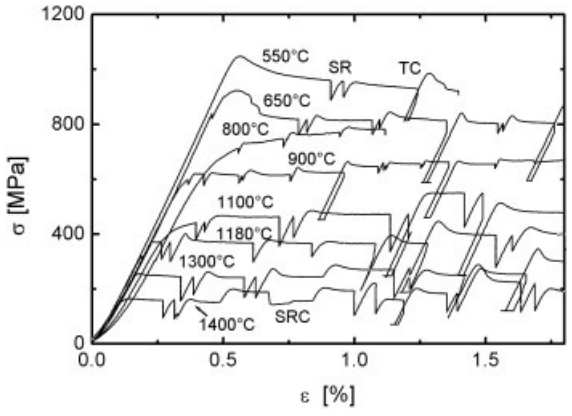


**Fig. 1** Stress-strain curves of $ZrO_2$-10 mol% $Y_2O_3$ deformed along ⟨100⟩ at a strain rate of $10^{-5}$ $s^{-1}$, including stress relaxation (SR), strain rate cycling (SRC) and temperature change (TC) tests.

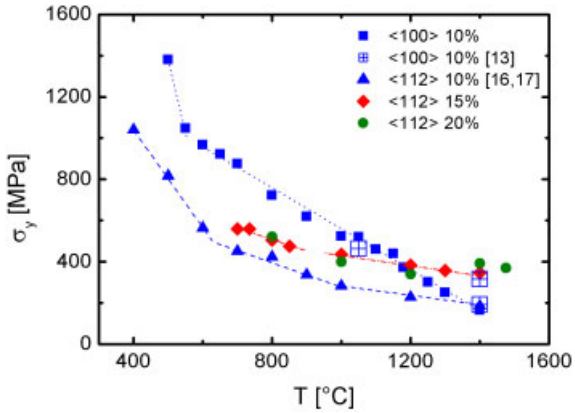


**Fig. 2** (online colour at: www.interscience.wiley.com) Flow stresses $\sigma_y$ versus temperature $T$ at a strain rate of $10^{-5}$ $s^{-1}$. Solid squares: $ZrO_2$-10 mol% $Y_2O_3$, ⟨100⟩ orientation. Diamonds: $ZrO_2$-15 mol% $Y_2O_3$, ⟨112⟩ orientation. Circles: $ZrO_2$-20 mol% $Y_2O_3$, ⟨112⟩ orientation. Triangles: $ZrO_2$-10 mol% $Y_2O_3$, ⟨112⟩ orientation, reference data from [16, 17] taken at a strain rate of $10^{-6}$ $s^{-1}$. Open squares plus crosses: $ZrO_2$-10 mol% $Y_2O_3$, ⟨100⟩ orientation, data from [13] taken at $10^{-6}$ $s^{-1}$ (1150 °C and 1400 °C) and $10^{-4}$ $s^{-1}$ (1400 °C).

All data in Fig. 2 can be divided into ranges of approximately linear dependencies of $\sigma_y$ on $T$. The respective values of the temperature sensitivity $\Delta\sigma/\Delta T$ are plotted in Fig. 3 as straight horizontal lines. $\Delta\sigma/\Delta T$ values have also been determined from temperature change tests as described in Section 2. These data are plotted as different symbols. At intermediate temperatures, the data from the $\sigma_y$ versus $T$ curves are approximately equal to the data from the temperature change tests. In the ⟨100⟩ compression direction, the temperature sensitivity is practically constant. For the ⟨112⟩ reference orientation, the temperature sensitivity decreases with increasing temperature. At high temperatures, however, temperature change tests yield a much higher temperature sensitivity than the slope of the $\sigma_y$ versus $T$ curves.

Figure 4 shows typical stress relaxation curves at different temperatures (full symbols) which were measured to determine the strain rate sensitivity $r$ of the flow stress. The relaxation rates plotted at the ordinate are proportional to the strain rates. Thus, these plots exhibit the dependence of the strain rate on the stress. Except at intermediate temperatures between about 1000 °C and 1250 °C, the curves are bent towards the stress axis. This is the normal shape characteristic, e.g., of the thermally activated overcoming of glide obstacles. At intermediate temperatures, however, the shape of the relaxation curves at low strains can be described either by an "inverse" curvature or by two distinct ranges, a steep range, stage 1, of low strain rate sensitivity at the beginning of the relaxation curves followed by a flat range, stage 2, of higher strain rate sensitivity. This has been observed before in zirconia at high temperatures [13]. Repeated relaxation curves (open symbols), which were taken immediately after the original relaxations without reaching steady state deformation again, start at significantly lower relaxation rates than the

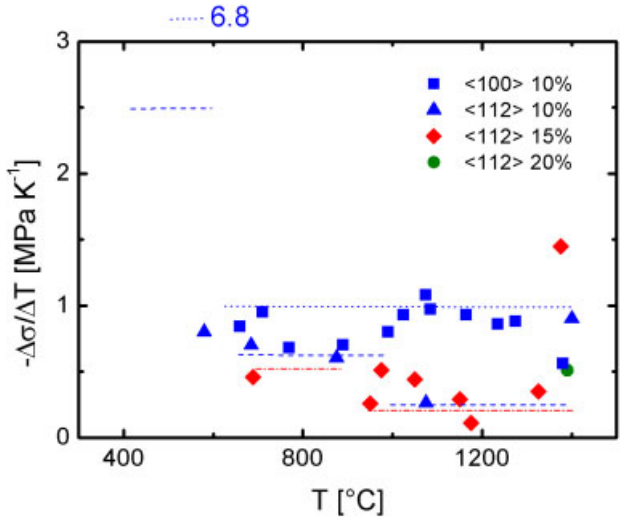


**Fig. 3** (online colour at: www.interscience.wiley.com) Temperature sensitivity of the flow stress as a function of temperature. Horizontal lines: data from the slopes of the straight lines in Fig. 2. Symbols as in Fig. 2: data from TC tests.

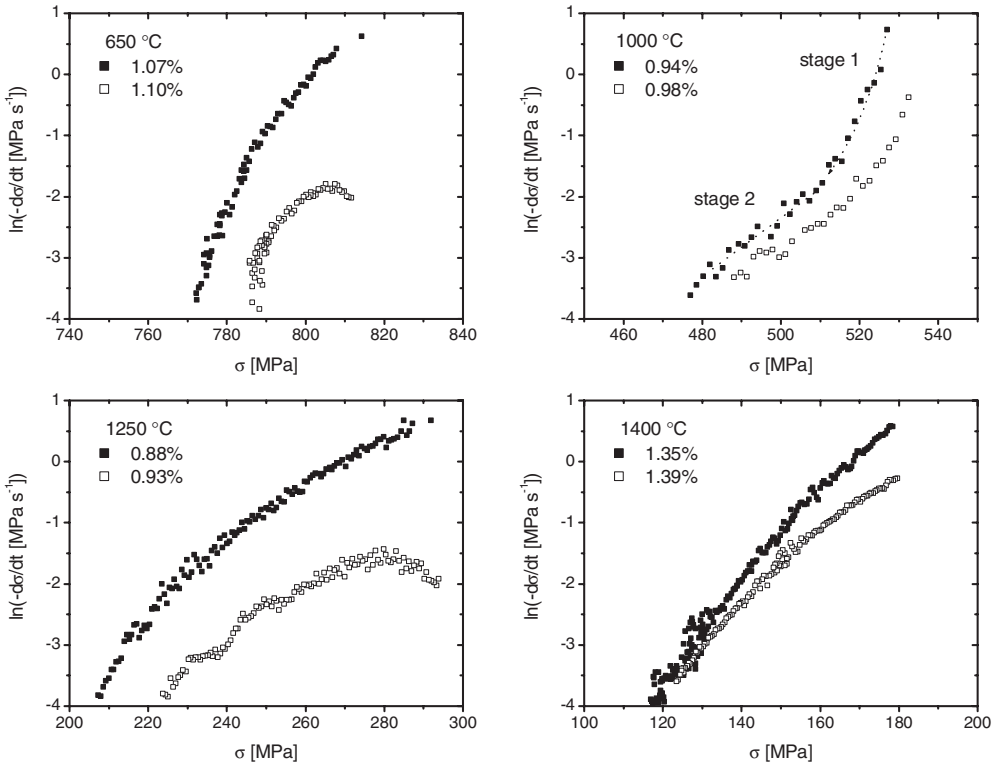


**Fig. 4** Stress relaxation curves at different temperatures. Full symbols: original relaxation curves. Open symbols: repeated relaxation curves.

original curves. At 650 °C and 1250 °C, the relaxation rate first increases before it decreases in the usual way. The differences between the original and repeated relaxation curves indicate changes in the microstructure or dislocation mobility during the relaxation tests. These changes are manifest in the yield drop effects occurring after all tests with partial unloading, i.e. stress relaxation and temperature change tests in Fig. 1. $r$ was usually determined from the slope of the original relaxation curves at the beginning of the relaxations. These values correspond to the conditions during steady state deformation just before the relaxations. The data are summarized as full symbols (squares) in Fig. 5 in a logarithmic scale. Since $r$ depends on the strain, the individual data are extrapolated to a plastic strain of 0.5%. A few strain rate sensitivity data were also obtained from strain rate cycling tests. They do not differ remarkably from those of the stress relaxation tests. In the intermediate temperature range, where the relaxation curves show the two ranges, the higher strain rate sensitivities corresponding to the flat stage 2 of the relaxation curves, i.e. to strain rates considerably lower than the rate before the relaxation test, are plotted as open symbols. The strain rate sensitivity starts with high values at low temperatures, goes through a minimum near 1000 °C and increases again at higher temperatures. The data measured along ⟨100⟩ approach those taken along ⟨112⟩ at low and high temperatures. They are distinctly higher by a factor of about 5 between about 800 °C and 1200 °C. At the soft ⟨112⟩ reference orientation, $r$ is very low at 1000 °C, only about 1 MPa.

The activation enthalpy $\Delta H$ of deformation was calculated by using Eq. (2). The data for specimens with 10 mol% deformed along ⟨100⟩ are plotted in Fig. 6. At low temperatures, $\Delta H$ increases rapidly with increasing temperature reaching about 10 eV at 800 °C and several tens of eV around 1000 °C. The very high values originate from the low strain rate sensitivity in this range. Between 1200 °C and

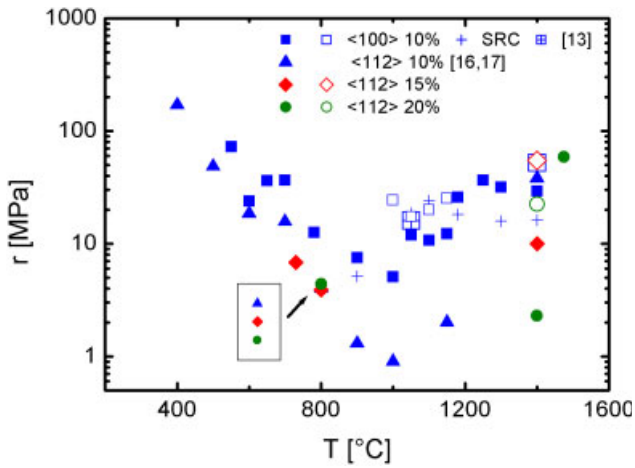


**Fig. 5** (online colour at: www.interscience.wiley.com) Strain rate sensitivity $r$ of the flow stress as a function of temperature. Symbols from SR tests as in Fig. 2. Full symbols: strain rate sensitivity at the beginning of the SR test. Open symbols: strain rate sensitivity during stage 2 of the relaxation curves. Crosses: SRC tests on $ZrO_2$-10 mol% $Y_2O_3$ deformed along ⟨100⟩. Open squares plus crosses: SR tests on $ZrO_2$-10 mol% $Y_2O_3$ deformed along ⟨100⟩ from [13].

1400 °C, $\Delta H$ is about 10 eV again. Except at high temperatures, the values for deformation along ⟨100⟩ are smaller than those along ⟨112⟩.

In the following, results are presented on the influence of yttria concentrations higher than 10 mol% on the deformation along the soft ⟨112⟩ orientation. Some stress-strain curves of $ZrO_2$-15 mol% $Y_2O_3$ are shown in Fig. 7. The material is brittle below about 700 °C even in the soft orientation. The deformation is stable at and below 800 °C and at and above 1400 °C but shows serrations at intermediate temperatures. These plastic instabilities will be discussed in Part II of this paper. The deformation curves of $ZrO_2$-20 mol% $Y_2O_3$ are similar except that the brittle-to-ductile temperature and the stability borders are shifted to somewhat higher temperatures. The temperature dependence of the yield stress of both materials is included in Fig. 2. Both materials show almost the same weak temperature dependence of the yield stress. At high temperatures, the yield stresses are higher than that of the 10 mol% material by a factor of two, but at low temperatures they approach that of the 10 mol% reference material. It follows from the straight lines in Fig. 2 that the temperature sensitivity of $ZrO_2$-15 mol% $Y_2O_3$ is less than that of $ZrO_2$-10 mol% $Y_2O_3$. The data are included in Fig. 3 together with those of the temperature change tests. Mostly both methods agree quite well. For the 20 mol% material, only a single temperature change test is available for about 1400 °C.

In the stable ranges of deformation, the stress relaxation curves of the materials with high yttria contents have mostly an inverse curvature but below a certain minimum rate, deformation becomes com-

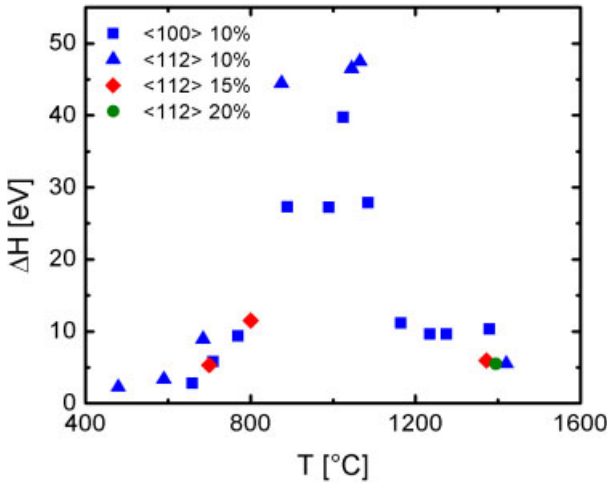


**Fig. 6** (online colour at: www.interscience.wiley.com) Activation enthalpy $\Delta H$ as a function of temperature.

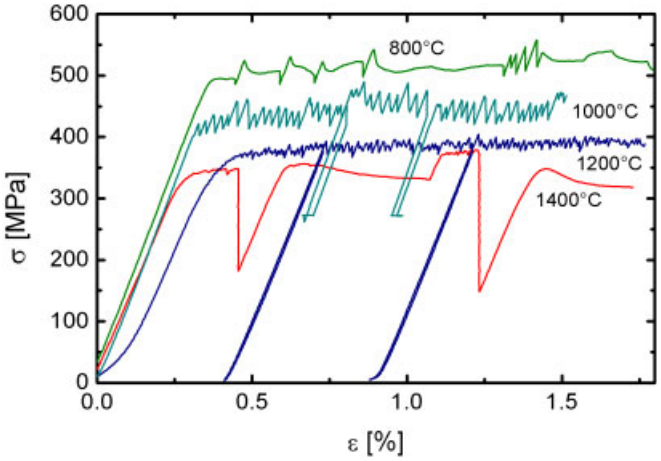


**Fig. 7** (online colour at: www.interscience.wiley.com) Stress-strain curves of $ZrO_2$-15 mol% $Y_2O_3$ deformed along ⟨112⟩ at a strain rate of $10^{-5}$ $s^{-1}$. The cusps in the curve of 800 °C correspond to SR and SRC tests.

pletely blocked. The strain rate sensitivity data are included in Fig. 5. In the stable low-temperature range, the $r$ values are almost equal to those of $ZrO_2$-10 mol% $Y_2O_3$ in the same orientation. At stable deformation at high temperatures, the $r$ values at the beginning of deformation are distinctly lower than those of the 10 mol% material, while the values of stage 2 (open symbols) are almost equal to them. In the instability range, strain rate sensitivity data were not calculated. The few activation enthalpy data of the 15 and 20 mol% materials are included in Fig. 6. They fit the values of the 10 mol% crystals.

### 3.2 Optical microscopy

Optical stress birefringence patterns give information on the slip systems activated and on the homogeneity of slip on a macroscopic level. Figure 8 presents such patterns for $ZrO_2$-10 mol% $Y_2O_3$ deformed along ⟨100⟩. At a temperature of 1100 °C, both cube side faces show well developed slip bands running in ⟨110⟩ directions (Fig. 8a). At the same time, slip steps on the surface observed by reflection microscopy run only in ⟨001⟩ directions. This is consistent with {110} planes being activated. At 1400 °C, slip has become very homogeneous (Fig. 8b).

In $ZrO_2$-15 mol% $Y_2O_3$ in the range of stable deformation at low temperatures, Lüders bands of the easy {100}1/2⟨011⟩ slip system start from places near the grip faces and extend over parts of the specimen length. In the instability range at 1000 °C, slip is localized in a few sharp slip bands (Fig. 9a). The

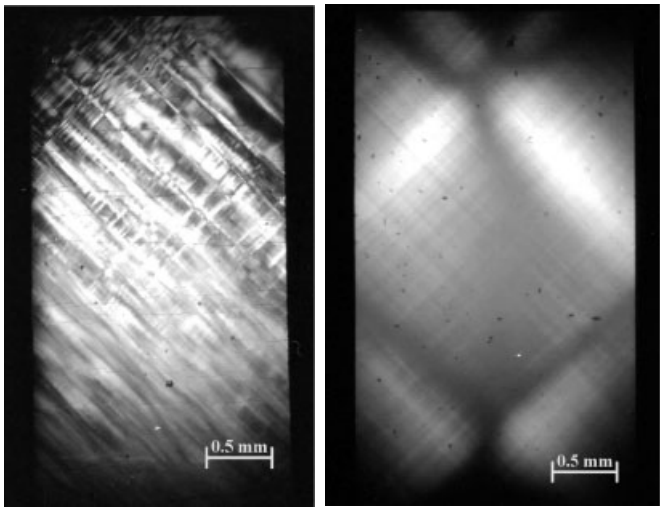


a) b)

**Fig. 8** Optical stress birefringence patterns on the {010} side faces of $ZrO_2$-15 mol% $Y_2O_3$ deformed along ⟨100⟩. a) 1100 °C, $\varepsilon = 2.5\%$. b) 1400 °C, $\varepsilon = 2.8\%$.

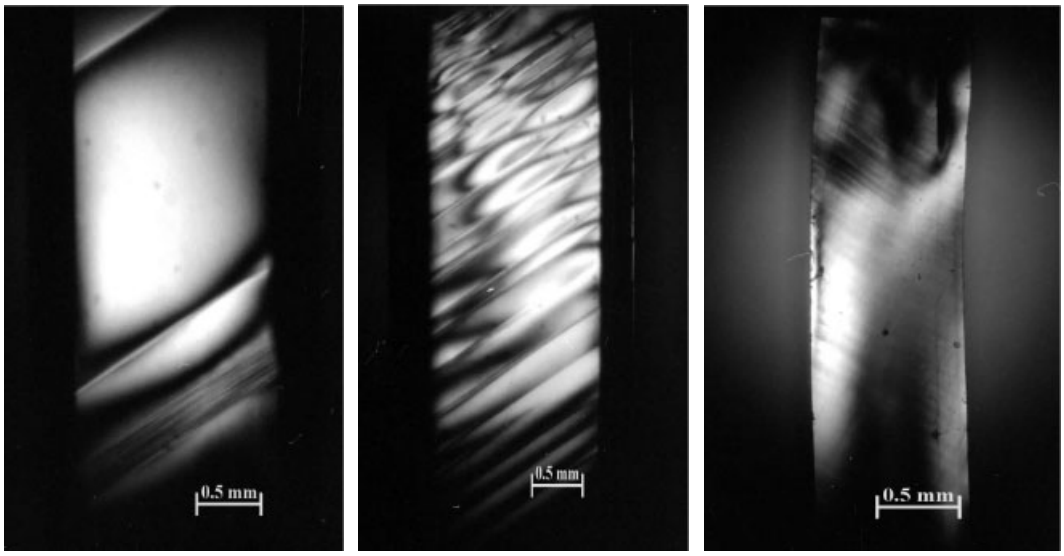


a) b) c)

**Fig. 9** Optical stress birefringence patterns on the {110} side faces of $ZrO_2$-15 mol% $Y_2O_3$ deformed along ⟨112⟩. a) 1000 °C, $\varepsilon = 1.5\%$. b) 1200 °C, $\varepsilon = 1.8$ %. c) 1400 °C, $\varepsilon = 3.5\%$.

angle of 54.7° of the band on the {110} face with respect to the compression direction and of 90° on the {111} face point at the easy slip system on a cube plane. At 1200 °C, a greater number of slip bands is distributed over the whole specimen length (Fig. 9b). In the stable range at 1400 °C, slip is homogeneous (Fig. 9c).

### 3.3 Transmission electron microscopy in the HVEM

All micrographs from $ZrO_2$-10 mol% $Y_2O_3$ deformed along ⟨100⟩ were taken near a ⟨001⟩ pole perpendicular to a {001} side face. In some cases, the directions of the Burgers vectors were determined using the $\boldsymbol{g} \cdot \boldsymbol{b} = 0$ contrast extinction rule. It was one aim of the microstructural investigations under the above deformation conditions to obtain information on the type of slip planes activated in the hard ⟨100⟩ orientation when the easy slip systems on cube planes have a zero orientation factor. Information on the slip planes can be obtained from the shape and orientation of the dislocations. In the projection onto the {001} side faces, for two of the four slip systems with {110} planes and orientation factors of $m_s = 0.5$ the slip planes are oriented edge on and the intersection lines with the surface run in ⟨110⟩ directions. For the remaining two systems, the slip planes are inclined by 45° with respect to the surface and the intersection lines run along ⟨100⟩ directions. The slip systems with the four {111} planes and orientation factors of 0.41 show all slip planes inclined by 54.7° with intersection lines running along ⟨110⟩.

Preparation of transmission electron microscopy specimens failed for samples deformed below 700 °C, because of the brittleness of the deformed material. At 700 °C (Fig. 10), slip is inhomogeneous, in accordance with the birefringence observations. In the upper part of the figure, dislocations look quite straight running in the two ⟨110⟩ directions on the surface plane. This is consistent with the arrangement of the dislocations on the {110} planes oriented edge on. In the lower part of the figure, dislocations are curved. The slip bands extend along the two ⟨110⟩ directions (the directions approximately perpendicular to the images of the dislocation lines which, mostly, cross the specimen with the shortest length on the slip plane). This points at the dislocations being arranged on {111} planes. Thus, slip systems with {110} and {111} planes coexist. This is characteristic for other temperatures, too.

Figure 11 displays a dislocation structure after deformation at 800 °C with two sets of dislocations, indicating multiple slip. At the (200) $\boldsymbol{g}$ vector in Fig. 11a, all dislocations are imaged with non-zero ori-

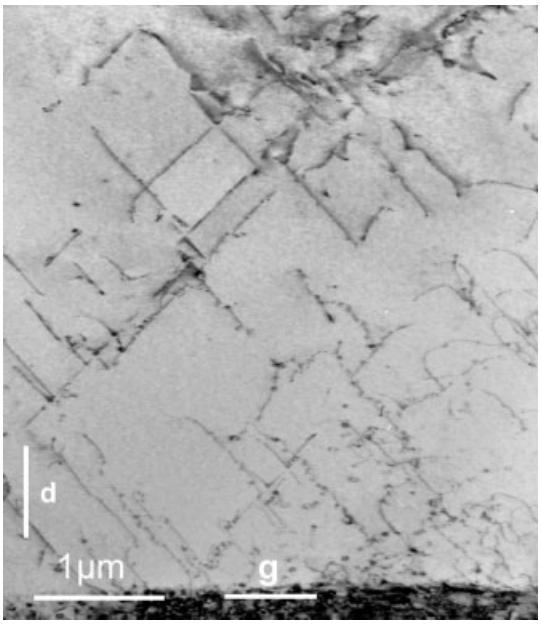


**Fig. 10** Dislocation structure of $ZrO_2$-10 mol% $Y_2O_3$ deformed along the compression direction $\boldsymbol{d}$ = [100] at 700 °C to a strain of 1.3%. Imaging diffraction vector $\boldsymbol{g}$ = (020) near the [001] pole. With this $\boldsymbol{g}$ vector, all dislocations of slip systems with non-zero orientation factors are visible.

entation factors. In Figs. 11b and c with $(2\bar{2}0)$ and (220) $\boldsymbol{g}$ vectors, always one set of dislocations with 1/2[110] and 1/2[$1\bar{1}0$] Burgers vectors within the image plane are extinguished. Since the dislocations have Burgers vectors in the image plane and are curved, they should be arranged on two of the {111} planes. The dislocations have a large screw component. The curved shape of the dislocations with cusps

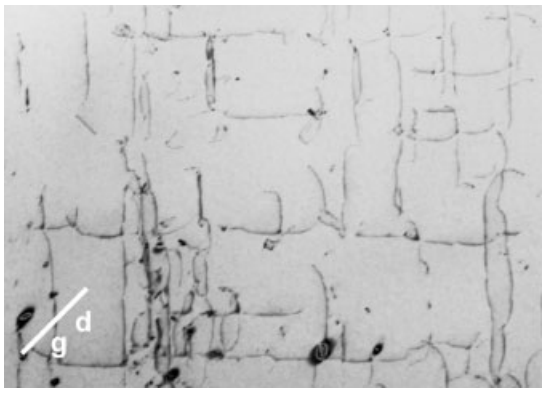


a)

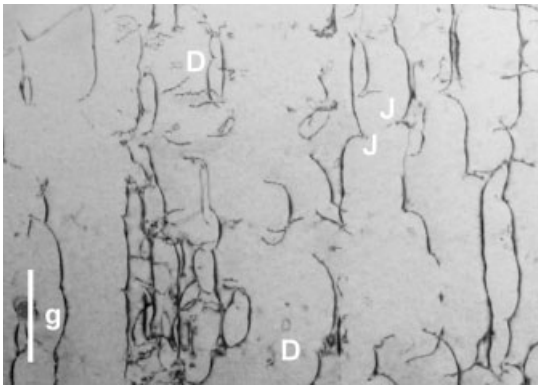


b)

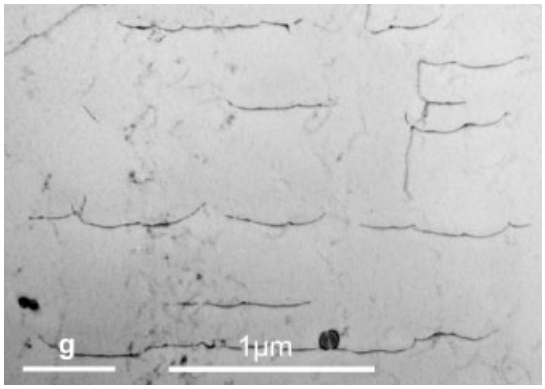


c)

**Fig. 11** Dislocation structure of $ZrO_2$-10 mol% $Y_2O_3$ deformed along $\boldsymbol{d}$ = [100] at 800 °C up to 1.1% imaged under different $\boldsymbol{g}$ vectors at the [001] pole. a) $\boldsymbol{g}$ = (200). b) $\boldsymbol{g}$ = $(2\bar{2}0)$. c) $\boldsymbol{g}$ = (220).

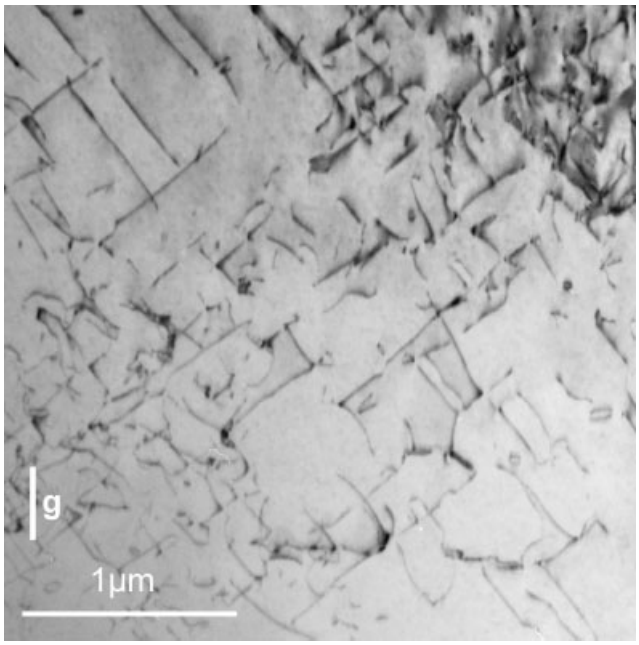


**Fig. 12** Dislocation structure of $ZrO_2$-10 mol% $Y_2O_3$ deformed along $\boldsymbol{d}$ = [100] at 1050 °C up to 1.8%. $\boldsymbol{g}$ = (200).

indicates that they are pinned by localized obstacles and bow out between them. Similar structures are formed also at 700 °C (Fig. 10) and 1050 °C (Fig. 12). Part of the cusps corresponds to high jogs. These jogs trail short dislocation dipoles of low contrast. Some of them are labelled J in Fig. 11b. The fraction of jogs with respect to the total number of cusps is not high. Besides, the density of debris produced by these jogs (marked D) is not high so that these processes should not essentially contribute to the flow stress.

At temperatures above about 1200 °C, slip becomes homogeneous and the pinned and bowed-out shape of the dislocations disappears (Fig. 13a, 1300 °C). They are now smoothly curved and have many triple nodes indicating that they form a three-dimensional network. The situation is similar at 1400 °C as demonstrated in Figs. 13b and c which show dislocations lying on the two sets of {110} planes oriented edge on.

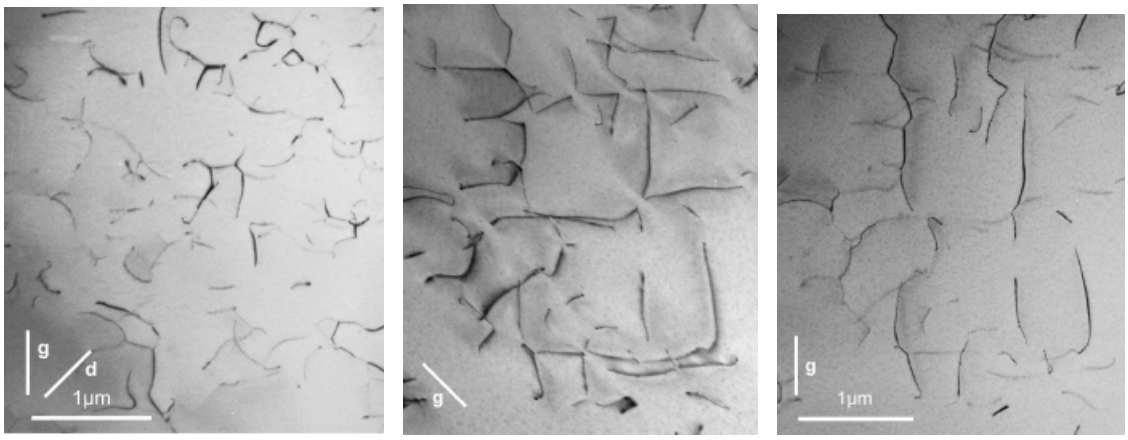


a) b) c)

**Fig. 13** Dislocation structure of $ZrO_2$-10 mol% $Y_2O_3$ deformed along $\boldsymbol{d}$ = [100] at high temperatures. a) 1300 °C, 2.6%. $\boldsymbol{g}$ = (220). b) 1400 °C, 2.6%, $\boldsymbol{g}$ = (020). c) Same area as b), $\boldsymbol{g}$ = (220).

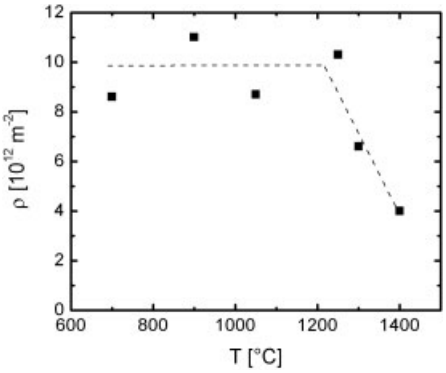


**Fig. 14** Dislocation density of $ZrO_2$-10 mol% $Y_2O_3$ deformed along ⟨100⟩ as a function of temperature.

Summarizing the qualitative observations, it may be stated that both {110} and {111} slip planes are activated at all temperatures during deformation along ⟨100⟩, where the easy slip systems with {100} planes are out of stress. Slip is localized at low temperatures and becomes homogeneous at high ones. Up to 1050 °C, the dislocations bow out between localized obstacles. At high temperatures, a dislocation network forms.

The dislocation density $\rho$ was measured from about four selected micrographs for each temperature by counting the numbers of intersections of the dislocation lines $N_1$ and $N_2$ with two orthogonal grids of straight lines of lengths $P_1$ and $P_2$ according to $\rho = (N_1/P_1 + N_2/P_2)/t$. The specimen thickness $t$ was estimated from the projected length of dislocations crossing the specimen on a known slip plane. As demonstrated in Fig. 14, the dislocation density is constant up to 1250 °C and decreases rapidly above this temperature.

In addition, the average length of bowed-out dislocation segments was determined from micrographs showing dislocations with well visible cusps as in Fig. 11. The average segment length was taken as evaluated dislocation line length $l_d$ per number of cusps $m$: $l_s = l_d/m$. The segment lengths are about 73 nm at 700 °C, 170 nm at 800 °C and 140 nm at 900 °C. At high temperatures, the dislocations are not pinned anymore, as stated above.

Some micrographs were also taken from a $ZrO_2$-15 mol% $Y_2O_3$ crystal deformed along ⟨112⟩ at 1200 °C (Fig. 15). Dislocations on the {100} easy slip plane are imaged edge-on and appear in very

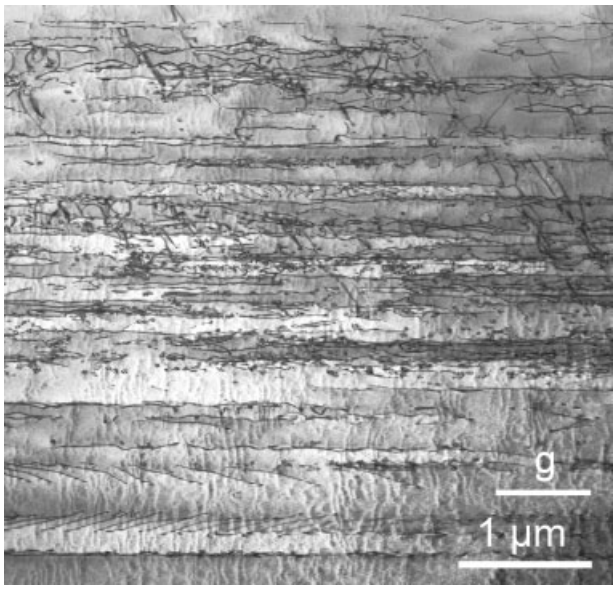


**Fig. 15** Dislocation structure of $ZrO_2$-15 mol% $Y_2O_3$ deformed along $\boldsymbol{d}$ = ⟨112⟩ at 1200 °C. ⟨110⟩ pole. $\boldsymbol{g}$ = (220).

narrow slip bands indicating planar slip. The broader bands contain dislocations belonging mostly to the {111} slip planes. Part of the dislocations of Burgers vectors of equal sign are arranged in planar groups. This is important with respect to the unstable deformation discussed in more detail in Part II of this paper.

## 4 Discussion

### 4.1 Slip systems

Slip on non-cube planes has previously only been studied at or around 1400 °C [6, 13, 23]. While slip on {111} was reported to be activated during deformation along ⟨100⟩ [6, 23], it is argued in [13] that {110} planes dominate. The flow stresses on {110} and {111} planes are supposed to be about 30% higher than that on {100} [6]. The present investigations on samples deformed at lower temperatures suggest that both slip planes, {110} and {111}, are activated in the whole temperature range. However, the difference of the flow stress with respect to the easy {100} plane becomes much greater at intermediate temperatures than at 1400 °C.

### 4.2 Activation parameters of the plastic deformation

In the model of thermally activated dislocation glide, the plastic strain rate is expressed by an Arrhenius type relationship

$$\dot{\varepsilon} = \dot{\varepsilon}_0 \exp(-\Delta G/kT) \tag{3}$$

with

$$\Delta G(\tau^*) = \Delta F(\tau^*) - V(\tau^*)\,\tau^*. \tag{4}$$

Here, $\dot{\varepsilon}_0$ is the pre-exponential factor containing the mobile dislocation density and the distance of forward jumps after successful thermal activation. $\dot{\varepsilon}_0$ is usually considered constant. $\Delta G$ is the Gibbs free energy of activation, $\Delta F$ the free energy of activation, $k$ Boltzmann's constant, $T$ the absolute temperature, $V$ the activation volume and $\tau^*$ the so-called effective (shear) stress. It is related to the total shear stress $\tau$ by

$$\tau = \tau_i + \tau^*. \tag{5}$$

$\tau_i$ is the athermal stress component resulting from long-range dislocation interactions. The activation volume $V$ is determined from the strain rate sensitivity $r$ by

$$V = kT/(m_s r)\,, \tag{6}$$

with $m_s$ being again the orientation factor relating the flow stress $\sigma$ to the shear stress $\tau = m_s\sigma$. According to Fig. 16, the activation volume of the 10 mol% yttria ⟨112⟩ reference specimen increases from a few $b^3$ at 400 °C to almost $1000b^3$ at 1000 °C. $b$ is the absolute value of the Burgers vector. These large values are not consistent with the model of thermal activation. Along ⟨100⟩, the activation volumes are always smaller than those along ⟨112⟩ with a maximum of $175b^3$. The few values of the materials with higher yttria concentrations fit those of the 10 mol% reference material in the same orientation.

At high temperatures, the strain rate sensitivity can be discussed in terms of the stress exponent

$$m^* = \mathrm{d}\ln\dot{\varepsilon}/\mathrm{d}\ln\sigma = \sigma/r. \tag{7}$$

Some values are listed in Table 1. At 1400 °C, they are all close to 6, except for the 20 mol% material which is not yet in the recovery range. However, $m^*$ becomes also equal to about 6 at a higher temperature.

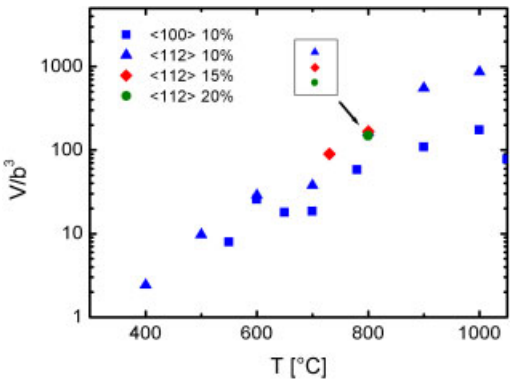


**Fig. 16** (online colour at: www.interscience.wiley. com) Dependence of the activation volume $V$ on temperature. Symbols as in Fig. 2.

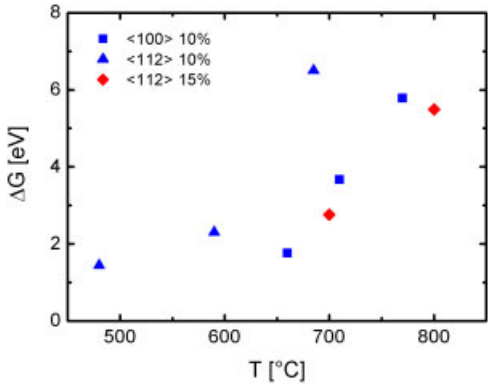


**Fig. 17** (online colour at: www.interscience.wiley.com) Gibbs free activation energy $\Delta G$ as a function of temperature. Symbols as in Fig. 2.

The Gibbs free energy of activation $\Delta G$ of Eqs. (3) and (4) can be calculated from the activation enthalpy $\Delta H$ in Fig. 6 using the formula of Schöck [24]

$$\Delta G = \Delta H - T\,\Delta S = \frac{\Delta H + \beta\tau V}{1-\beta} = \frac{\Delta H + \beta kT\sigma/r}{1-\beta}, \tag{8}$$

where $\Delta S$ is the activation entropy, $\mu$ the shear modulus and $\beta = (T/\mu)\,(\mathrm{d}\mu/\mathrm{d}T)$. The formula contains only measurable quantities and is based on the assumption that the only contributions to the entropy arise from the temperature dependence of the shear modulus. For the present evaluations, $\mu$ was substituted by the energy factor $K_s$ of screw dislocations with $a/2\langle 110\rangle$ Burgers vectors calculated in [25] by anisotropic elasticity theory using the temperature depending elastic constants from [26]. The result is shown in Fig. 17 for temperatures up to 800 °C. According to Eq. (3), $\Delta G$ should be proportional to $T$ if the deformation is controlled by a single thermally activated process. For all specimens, $\Delta G$ increases with temperature, but much more strongly than predicted for a single process. Thus, the controlling process may change within the discussed temperature range. Values of $\Delta G$ are not calculated for temperatures above 800 °C. The large values around 1000 °C are not consistent with thermally activated dislocation motion. The discussion of the recovery range at high temperatures is based on $\Delta H$.

In the following, the different mechanisms contributing to the flow stress are discussed. This is based on the earlier considerations in [11, 13, 16, 17, 19, 25] and reviewed in [20].

### 4.3 The athermal stress component $\tau_i$

Long-range interactions between the dislocations cause an athermal component $\tau_i$ of the flow stress. One contribution to this component is the stress arising from the mutual elastic interaction between parallel

**Table 1** Stress exponent $m^*$ of the plastic strain rate in stage 2 according to Eq. (7) at high temperatures.

| specimen | $T$ [°C] | $\sigma$ [MPa] | $r$ [MPa] | $m^*$ |
|---|---|---|---|---|
| ⟨100⟩ 10% | 1400 | 165 | 29.2 | 5.7 |
| ⟨112⟩ 10% | 1400 | 184 | 38 | 4.8 |
| ⟨112⟩ 15% | 1400 | 345 | 54.8 | 6.3 |
| ⟨112⟩ 20% | 1400 | 392 | 22.5 | 17.4 |
| ⟨112⟩ 20% | 1475 | 370 | 58.8 | 6.3 |

dislocations called Taylor hardening [27]. Using anisotropic elasticity, the stress contribution $\tau_p$ from parallel dislocations can be written as [25, 20]

$$\tau_p = \alpha K b F_m \rho^{1/2}/(2\pi) \,, \tag{9}$$

where $\alpha$ is a numerical constant of about 8, K again the energy factor of the dislocations, $F_m$ a dimensionless maximum interaction force and $\rho$ the dislocation density. Since the dislocations have mostly screw character, $K$ and $F_m$ were selected for screw dislocations. For 700 °C, they amount to $K_s$ = 80.4 GPa and $F_{ms}$ = 0.30 for {100} planes (⟨112⟩ orientation of compression axis) and $F_{ms}$ = 0.66 for {111} planes (⟨100⟩ orientation) [25, 20]. Unfortunately, values of $F_m$ are not available for {110} planes. Taking the dislocation densities for $ZrO_2$-10 mol% $Y_2O_3$ for the ⟨112⟩ compression direction from [16] and for the ⟨100⟩ direction from Fig. 14, the dependence of $\tau_p$ on the temperature is shown in Fig. 18. The values are slightly greater for the ⟨100⟩ orientation, owing to the greater $F_m$ value. They are compared with the total (shear) flow stress $\tau_y$ calculated from $\sigma_y$ with the orientation factors of the respective slip systems. In the athermal range around 1000 °C of the ⟨112⟩ reference specimens, $\tau_p$ amounts to about 40 MPa. It is shown by *in situ* straining experiments in an HVEM [22] that the dislocations move very jerkily and bow out between large jogs. At 1150 °C, this process causes a back stress $\tau_b$ of about 75 MPa [20], which also contributes to the athermal stress component $\tau_i$. Thus, $\tau_i = \tau_p + \tau_b \cong$ (40 + 75) MPa, which just equals the macroscopic flow stress. The athermal nature of the flow stress of $ZrO_2$-10 mol% $Y_2O_3$ around 1000 °C along ⟨112⟩ is in agreement with the low strain rate sensitivity (or the large activation volume, Fig. 16) and the very large experimental activation energy (Fig. 6).

At deformation along ⟨100⟩, *in situ* straining experiments show dislocations moving continuously on {110} planes also bowing out to similar curvatures as during deformation along ⟨112⟩ [22]. It may therefore be concluded that the back stress $\tau_b$ and accordingly also the total athermal stress component $\tau_i$ has a similar magnitude as along ⟨112⟩. In this case, however, the (shear) flow stress at 1000 °C is about 200 MPa. Thus, the Taylor hardening component amounts only to about 60% of the flow stress. At the ⟨100⟩ compression axis, multiple slip occurs, as demonstrated by Fig. 11. This may induce both an additional athermal and a thermal flow stress component. Nevertheless, the influence of thermal activation on the flow stress along ⟨100⟩ is documented by the smaller activation volume (Fig. 16) and the high temperature sensitivity of the flow stress (Figs. 2 and 3).

It may be concluded that the athermal processes yield an important component $\tau_i$ to the flow stress, in particular around 1000 °C. Since it increases only slightly with decreasing temperature, it becomes less important at lower temperatures where the total flow stress increases strongly. Unfortunately, neither dislocation density data nor results from *in situ* experiments are available yet for the deformation of specimens with higher yttria concentrations. Probably, $\tau_i$ is slightly higher because of higher dislocation densities in the localized slip bands but the ratio between $\tau_i$ and $\tau_y$ may be similar to that of the 10% material.

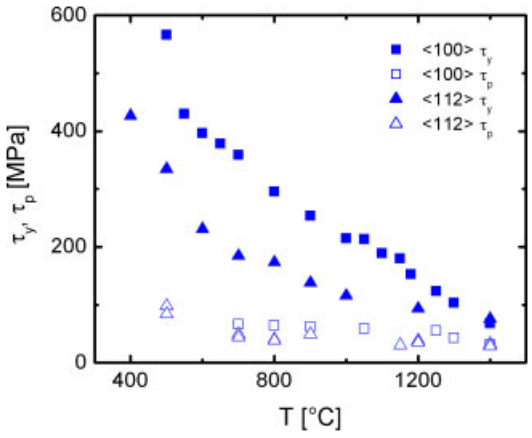


**Fig. 18** (online colour at: www.interscience.wiley.com) Critical resolved shear stress $\tau_y$ of $ZrO_2$-10 mol% $Y_2O_3$ deformed along ⟨100⟩ (solid squares) and ⟨112⟩ (solid triangles) and athermal flow stress component $\tau_p$ from long-range interaction between parallel dislocations (corresponding open symbols) as a function of temperature.

### 4.4 The Peierls mechanism

The steep increase of the flow stress of the 10 mol% reference material deformed along ⟨112⟩ below about 500 °C (Fig. 2), particularly if the data measured under confining hydrostatic pressure from [18] are included, and the related strong increase of the strain rate sensitivity (Fig. 5) were interpreted in [17, 19] by a transition to the action of the Peierls mechanism. As shown in Fig. 16, the large strain rate sensitivity below 500 °C corresponds to activation volumes below about $10b^3$, which are well consistent with the Peierls mechanism. Specimens deformed along ⟨100⟩ show also a steep increase of the flow stress at 500 °C and the activation volumes approach, at low temperatures, the values in the soft orientation. Thus, the Peierls mechanism should also be active on the non-cube slip planes at low temperatures. The fact that the bowed-out shape of dislocations between obstacles is preserved in the unloaded specimens (Figs. 10 and 11) points at a friction mechanism being active also at temperatures higher than 500 °C. However, the Peierls mechanism seems not to be responsible for the difference in the flow stress for slip on cube or non-cube planes (for the two loading directions) in a wide range of temperatures, since above about 800 °C the activation volumes are too large for this mechanism (Fig. 16). The specimens with yttria concentrations higher than 10 mol% broke before the range of the Peierls mechanism was reached.

### 4.5 Elastic interactions between dislocations and point defects

Originally, the dependence of the flow stress of cubic zirconia on the stabilizer content at 1400 °C was interpreted by solution hardening, i.e. by the elastic interaction between the dislocations and the yttrium ions, their charge compensating oxygen vacancies or agglomerates of them (e.g. [2]). There is a remarkable difference in the ionic radii of the yttrium and zirconium ions which may lead to solution hardening owing to the size misfit. Estimations about this contribution to the flow stress are given in the Appendix. As shown there, the size misfit interaction can yield a considerable contribution to the flow stress of $ZrO_2$-10 mol% $Y_2O_3$ in a wide range of temperatures and therefore also to the materials with higher yttria concentrations. Also the order of magnitude of the predicted activation volume fits the range of experimental values (Fig. 16). However, this model does not agree with the functional dependencies. The experimental activation volume depends on the temperature much more strongly than predicted theoretically. Besides, it should be inversely proportional to the square root of the yttrium concentration instead of being independent of it. In particular, the obstacle distances in the range of 100 nm observed by transmission electron microscopy in Section 3.3. disagree with the very short distances between the individual yttrium ions of only a few $b$. It may therefore be concluded that direct solution hardening by the solved yttrium ions yields only a small contribution to the flow stress.

Agglomerates of yttrium ions and oxygen vacancies form electric and elastic dipoles, which have been proved by mechanical loss spectroscopy [28–30]. Since the mobility of the oxygen vacancy near the yttrium ion is very high, the relaxation maxima are below 400 °C, i.e. these defects do not act as fixed obstacles in the range of the present experiments. The respective reorientation processes might lead to the induced Snoek effect in the temperature range of the relaxation maxima, i.e. also below the present temperature range. At higher temperatures, the agglomerates dissociate [30–32]. In tetragonal zirconia polycrystals with 3 mol% $Y_2O_3$, the dissociation takes place between 520 °C and 650 °C [31]. At higher $Y_2O_3$ concentrations the dissociation is shifted to higher temperatures (e.g. [30]). It is argued in [33] that part of the yttrium ions are associated with vacancies even at 1400 °C and that the concentration of free yttrium ions in % is given by $c_{Y_{3+}} \cong 2.47\, c_{Y_2O_3}^{0.71}$, where $c_{Y_2O_3}$ are the mole% of $Y_2O_3$. Perhaps the oxygen vacancies balance the size misfit of the yttrium ions so that the associates have only a weak size misfit interaction with the dislocations.

### 4.6 Precipitation hardening

Plastic deformation in the temperature range between about 500 °C and 800 °C seems to be essentially controlled by precipitation hardening. The flow stress exhibits a moderate temperature sensitivity (Figs. 2

and 3) and the strain rate sensitivity (Fig. 5) corresponds to activation volumes of some tens to some hundreds of $b^3$ (Fig. 16). The Gibbs free energy takes reasonable values mostly below 6 eV (Fig. 17). As discussed already in Section 4.2, the increase of the activation energy with temperature is too strong for a single thermally activated process so that another thermally activated process should be superimposed, probably the Peierls mechanism at low temperatures. The occurrence of precipitation hardening is supported by the bowed-out shape of the dislocations in the respective temperature range (Figs. 10 and 11). As described in Section 3.3 for *c*-$ZrO_2$-10 mol% $Y_2O_3$ along ⟨100⟩, the distance $l$ between these obstacles ranges between 73 and 170 nm depending on the temperature, which corresponds to 200 … 460$b$. In the model of localized obstacles, the activation volume is given by $V = (2/3)\ lbd$, where $d$ is the so-called activation distance, i.e. the effective width of the obstacles at the given stress. The factor 2/3 originates from the Friedel statistics appropriate for randomly arranged strong obstacles. The present data yield $d = 0.15 \ldots 0.3b$. Since the precipitates are certainly much larger, this indicates that the effective forces on the obstacles almost reach the obstacle strength so that only the tips of the obstacles are overcome by thermal activation. As shown in Fig. 16, the activation volume is not influenced by the yttria concentration. Thus, the precipitates should not be connected with the yttria stabilizer. Unfortunately, only a hypothesis can be presented about the nature of the precipitates. According to [33], high concentrations of nitrogen are solved in zirconia crystals owing to their growth in air, which precipitate at high temperatures to form ZrN particles. In the system $ZrO_2$–ZrN (i.e. without yttrium), the structure of precipitates has been studied in [34]. Crystals containing more than 2.5 mol% ZrN show small precipitates either of tetragonal or monoclinic structure. The precipitates are coherent with their tetragonal *c*-axis or their monoclinic *c* or *b*-axes parallel to a cube direction of the matrix. In addition, the monoclinic particles are heavily twinned with {100} or {110} twin planes (in cubic notation). Thus, the structure of these precipitates resembles that of the tetragonal precipitates in partially stabilized zirconia. Since the ZrN precipitates occur at all yttria concentrations studied in [33] and since the crystal material was supplied by the same company for the study in [33] and the present one, it is believed that small particles containing nitrogen cause the precipitation hardening in the temperature range between 500 °C and 800 °C.

The difference in the flow stresses of $ZrO_2$-10 mol% $Y_2O_3$ deformed along ⟨100⟩ in comparison to ⟨112⟩ at intermediate temperatures should be related to the dominating thermally activated mechanism, i.e. to precipitation hardening, since the strain rate sensitivity is much higher along ⟨110⟩ than along ⟨112⟩. The obstacle distances, however, are practically equal in both directions (compare the values above with Fig. 8 in [17]) in agreement with the fact that the dislocations interact with the same obstacles in both orientations. An equal obstacle distance $l$ but a smaller activation volume $V$ along ⟨100⟩ (Fig. 16) result in a smaller value of the activation distance $d$. At the same time, also the Gibbs free energy of activation $\Delta G$ is lower (Fig. 17). This is consistent with different interaction profiles of the same obstacles on different slip planes with similar total activation energies. At the more narrow profile for non-cube slip at the ⟨100⟩ compression direction, the acting force and thus the effective stress must be higher to arrive at smaller values of d and $\Delta G$. According to Eq. (3), however, the different values of $\Delta G$ from Fig. 17 yield pre-exponential factors $\dot{\varepsilon}_0$ differing by many orders of magnitude, which is very unrealistic.

In principle, different activation parameters of overcoming the same precipitates on different slip planes can be understood on the basis of the suggestion above that the obstacles are coherent particles of different crystal structure. If the dislocations of the matrix cut these particles, antiphase boundary-like defects have to be created, which impede the motion of the dislocations inside the particles. Since the energies of these faults may depend on the plane, different interaction forces with dislocations will result. Thus, the bowed-out shape of dislocations and the values of the activation volume clearly indicate the action of precipitation hardening in the discussed temperature range, but the details of this mechanism are not well understood. While for the reference specimens of $ZrO_2$-10 mol% $Y_2O_3$ deformed along ⟨112⟩, this mechanism ceases in the athermal range around 1000 °C, it seems still to operate at these temperatures for deformation along ⟨100⟩. The contribution of precipitation hardening seems to be independent of the stabilizer concentration. Thus, it does not explain the higher flow stress of the materials with higher yttria concentrations.

### 4.7 Formation of solute atmospheres on dislocations (dynamic strain ageing)

While along ⟨112⟩ the $ZrO_2$-10 mol% $Y_2O_3$ crystals show athermal deformation behaviour around 1000 °C with very low strain rate sensitivities, specimens with 15 and 20 mol% exhibit plastic instabilities in this temperature range. This is usually interpreted by the so-called Portevin–LeChatelier (PLC) effect [35] or dynamic strain ageing leading to a locking of the dislocations and to an additional contribution to the flow stress. It is argued in Part II of this paper that the effect is caused by short-range diffusion of unassociated yttrium ions. Thus, this process may result in the difference between the flow stresses of $ZrO_2$-10 mol% $Y_2O_3$ and the materials with higher yttria concentrations between about 800 °C and 1200 °C.

### 4.8 Recovery-controlled deformation at high temperatures

The deformation of *c*-$ZrO_2$ at temperatures around 1400 °C was discussed in detail in terms of recovery-controlled glide in [13], after the original suggestion in [11]. Similar views were also expressed, e.g., in [8]. As the work-hardening is low, the high-temperature deformation can conveniently be treated in terms of an equation for steady state creep (for a review concerning ceramics, see [36])

$$\dot{\varepsilon}_{ss} = A \frac{\mu b}{kT} \left( \frac{\sigma}{\mu} \right)^n D_0 \exp\left( -\frac{\Delta H}{kT} \right), \tag{10}$$

where $A$ is a dimensionless constant, $n$ the stress exponent for creep, $D_0$ the pre-exponential factor and $\Delta H$ the activation enthalpy of the respective diffusion process.

The relation between the steady state behaviour as in Eq. (10) and the transient behaviour like that during stress relaxation tests can be discussed by a model in [37, 38] where high-temperature deformation is described by a dynamic law of the dependence of the strain rate on the effective stress (analogous to Eqs. (3) and (4)) in form of a power law with the dynamic stress exponent $m$ and a law of the evolution of a threshold stress owing to the dislocation structure including a strain softening exponent $p$. As described in Section 3.1, stress relaxation curves may show two ranges, a steep one (stage 1: Fig. 4b, full symbols in Fig. 5) at the beginning and a flat one (stage 2, open symbols) corresponding to lower strain rates. This holds for $ZrO_2$-10 mol% $Y_2O_3$ deformed along ⟨100⟩ between 1000 °C and 1200 °C but in particular for the two materials with higher yttria concentrations along ⟨112⟩ at 1400 °C. The 10 mol% material shows only stage 2 because of the lower strain rate of this data set. In the model outlined above, in stage 1 the dynamic exponent m is approximately equal to the experimental stress exponent $m^*$ after Eq. (7) , i.e. it is given by the strain rate sensitivity $r$ and corresponds to the activation volume in Eqs. (4) and (6). These $r$ values are low owing to the athermal character of the dislocation motion as in the range around 1000 °C. Stage 2 corresponds to deformation controlled by dynamic recovery where the stress exponent $m^*$ is approximately equal to the softening exponent $p$ and also the creep exponent $n$ in Eq. (10). As listed in Table 1, the $m^*$ values of range 2 at 1400 °C are between 4.8 and 6.3, except for $ZrO_2$-20 mol% $Y_2O_3$ which reaches $m^* = 6.3$ only at 1475 °C. According to Table 1 of the review on creep of ceramics [36], the stress exponents of different mechanisms based on bulk diffusion range between 3 and 4.5 and are 5 or 6 for pipe diffusion. The present values approach these theoretical values.

For deformation along ⟨112⟩, the activation enthalpies at about 1400 °C amount to 5.5 to 6 eV (Fig. 6). This is close to the values of cation self diffusion in the bulk. For creep processes, diffusion must take place in both sublattices but is controlled by the slower moving species, i.e. the cations. The activation energy of self diffusion of $Zr^{4+}$ was thought to be identical with that of the Zr–Hf interdiffusion of 4.05 eV [39]. However, tracer diffusion measurements yielded 4.7 eV [40]. According to a dislocation loop shrinkage study in the lower temperature range between 1100 °C and 1300 °C, the activation energy (of climb) is 5.3 eV [12, 41]. Certainly, the latter study fits best the situation of the present experiments. Thus, both the stress exponent and the activation energy of the deformation around 1400 °C are close to the values suggested theoretically for recovery-controlled deformation. While the activation energy of cation diffusion seems to be independent of the stabilizer ions and concentration, the diffusion coeffi-

cient decreases by more than an order of magnitude by increasing the yttria concentration from about 10 to about 20 mol% [12, 40]. This dependence explains the increased flow stress of the materials with higher yttria concentrations where recovery is suppressed. $ZrO_2$-10 mol% $Y_2O_3$ exhibits equal flow stresses at the different loading axes since recovery effects are independent of the loading axis. If the occurrence of the two-stage stress relaxation curves is interpreted as an indication of recovery, recovery processes extend to lower temperatures for deformation along ⟨112⟩.

The influence of recovery is also obvious in the dislocation microstructure. At high temperatures, the dislocations are arranged in a three-dimensional network (Fig. 13). Besides, the dislocation density decreases drastically at high temperatures (Fig. 14). However, this may partly be an artefact owing to static recovery during cooling [13].

## 5 Conclusions

– At all temperatures, part of the flow stress is of athermal nature due to long-range interactions between dislocations and to the back stress of segments bowing out between large jogs or dislocation nodes. This contribution is responsible for the athermal deformation of $ZrO_2$-10 mol% $Y_2O_3$ along ⟨112⟩ around 1000 °C. In all other cases with higher flow stresses, other mechanisms are superimposed.

– At the lowest temperatures of this study, the Peierls mechanism causes a steep increase of the flow stress and the strain rate sensitivity for glide on both the cube slip planes (activated in the ⟨112⟩ orientation) and the non-cube slip planes (activated in the ⟨100⟩ orientation).

– Although solution hardening from the yttrium ions may theoretically yield a large contribution to the flow stress, the temperature range between 500 °C and 800 °C with activation volumes of up to more than $100b^3$ and dislocations pinned between obstacles about 130 nm apart can best be interpreted by the action of precipitation hardening. According to equal activation volumes for the materials with different yttria contents deformed along the soft ⟨112⟩ orientation, this mechanism does not cause the dependence of the flow stress on the yttria concentration at intermediate temperatures. It should, however, be responsible for the higher flow stress and the smaller activation volume of non-cube slip at deformation along ⟨100⟩.

– The formation of yttrium ion atmospheres in the dislocation cores may give rise to the higher flow stress of the materials with higher yttria contents due to strain ageing with serrated yielding at temperatures around 1000 °C. Details will be described in Part II of this paper.

– Around 1400 °C, deformation is controlled by recovery. As the diffusional recovery processes are little influenced by the slip system, the flow stress is equal for deformation of $ZrO_2$-10 mol% $Y_2O_3$ along ⟨112⟩ and ⟨100⟩. On the other hand, the decrease of the cation diffusion coefficient with increasing yttria concentration results in the higher flow stress of the materials with higher yttria contents at 1400 °C owing to reduced recovery.

## 6 Appendix

### 6.1 The contribution of solution hardening to the flow stress

In the following, the effect of solid solution hardening is estimated which occurs by the incorporation of yttria into the zirconia matrix. The atomic fractions of the yttrium ions with respect to the zirconium sites are $c$ = 0.182, 0.261 and 0.333 for the yttria concentrations of 10, 15 and 20 mol%. According to [A1], the ionic radius of $Y^{3+}$ at a coordination number of 8 amounts to 0.102 nm and that of $Zr^{4+}$ at the same coordination to 0.084 nm. This yields a size misfit of $\delta = 0.214$. The size misfit results in a parelastic interaction with the dislocations having a maximum interaction force [A2]

$$F_0 \cong 0.2\mu b^2 \delta . \tag{A1}$$

$\mu$ is the shear modulus, which is set equal to the energy factor $K_s$ of screw dislocations as in Sections 4.2. and 4.3. A value of 80.4 GPa is taken for 700 °C. With this value, there follows $F_0 = 4.63 \times 10^{-10}$ N.

For a triangular interaction potential and a width of the solute of $b$, the total activation energy is

$$\Delta G_0 = 0.5 F_0 b \,, \tag{A2}$$

which amounts to 0.53 eV.

The contribution of solid solution hardening to the (shear) flow stress at zero temperature is then given by the statistical theory [A3] as

$$\tau_{so} = 0.94(1 + 2.5\eta_0)^{1/3}\, c^{1/2} F_0^{3/2}/(b^2[2\Gamma]^{1/2}) \,. \tag{A3}$$

Here, $c$ is the atomic fraction of the solute and $\Gamma$ is the line tension. For a rough estimate, $\Gamma = 0.5 K_s b^2$ may be taken, which gives $\Gamma = 5.4 \times 10^{-9}$ N. $\eta_0$ is a normalized obstacle width, which is defined by

$$\eta_0 = y_0/b(2c\Gamma/F_0)^{1/2} \,. \tag{A4}$$

$y_0$ is the width of the interaction between the solute and the dislocation along the coordinate of forward motion, which was set equal to $b$ for individual yttrium ions. For the 10 mol% crystals, taken as an example, $\eta_0$ equals 2.1. This characterizes the solutes as relatively weak localized obstacles. The contribution of solid solution hardening at zero temperature turns out to be $\tau_{so} \cong 510$ MPa. In the theory of solution hardening [A3], the flow stress at a finite temperature depends on the total interaction energy $\Delta G_0$ between solutes and dislocations and the normalized obstacle width $\eta_0$. $\Delta G_0$ determines a characteristic temperature of the interaction between individual solutes and dislocations

$$T_0 = \Delta G_0/(k \ln [\dot{\varepsilon}_0/\dot{\varepsilon}]) \,. \tag{A5}$$

With the value of $\Delta G_0$ above, this corresponds to $T_0 = 307$ K, if $\ln [\dot{\varepsilon}_0/\dot{\varepsilon}] \cong 20$ is taken. According to the theory, the effective activation energies are larger than the energy $\Delta G_0$ to overcome a single solute and are given by $\Delta G_{eff} = \Delta G_0 T/T_0$. Some values are presented in Table A1. Figures 4 and 5 of [A3] describe the temperature dependence of the contribution of solution hardening $\tau_s$ to the flow stress normalized by $\tau_{so}$ and of a normalized activation volume $V/V_0$ as a function of $T/T_0$ with $\eta_0$ as a parameter. Some values, again for the $\eta_0$ value of the 10 mol% crystal, are also quoted in Table A1. The normalizing constant $V_0$ is given by

$$V_0 = g b^3 \eta_0/c \,, \tag{A6}$$

where $g$ is a constant close to unity. For the 10 mol% material, $V_0$ equals $11.7 b^3$. Though the yttrium ions, owing to their size misfit, should represent only weak obstacles to dislocation glide, they may cause a remarkable contribution to the flow stress because of their large concentrations. According to this theory, the flow stress is roughly proportional to $c^{1/2}$ and the activation volume to $c^{-1/2}$.

[A1] Handbook of Chem. & Phys., edited by D. R. Lide, CRC Press, Boca Raton et al., 1999.
[A2] D. Hull and D. J. Bacon, Introduction to Dislocations, Pergamon Press 1994.
[A3] R. Labusch and R. Schwarz, in: Strength of Metals and Alloys, edited by D. G. Brandon, R. Chaim and A. Rosen, Freund Publ. (London, 1991) p. 47.

**Table A1** Theoretical data for solution hardening in $ZrO_2$-10 mol% $Y_2O_3$.

| $T$ [°C] | $T/T_0$ | $\Delta G_{eff}$ [eV] | $\tau_s/\tau_{so}$ | $\tau_s$ [MPa] | $V/V_0$ | $V/b^3$ |
|---|---|---|---|---|---|---|
| 600 | 2.84 | 1.5 | 0.3 | 153 | 10 | 117 |
| 800 | 3.5 | 1.86 | 0.26 | 133 | 12.5 | 146 |
| 1000 | 4.15 | 2.2 | 0.23 | 117 | 14 | 164 |

**Acknowledgement** The authors are grateful for the cooperation within the framework of the Graduiertenkolleg No. 415 of the Martin-Luther-Universität Halle/Wittenberg and for its financial support by the Deutsche Forschungsgemeinschaft (A.T.).

## References

[1] A. Dominguez-Rodriguez, V. Lanteri, and A. H. Heuer, J. Am. Ceram. Soc. **69**, 285 (1986).
[2] A. Dominguez-Rodriguez, K. P. D. Lagerlöf, and A. H. Heuer, J. Am. Ceram. Soc. **69**, 281 (1986).
[3] E. Fries, F. Guiberteau, A. Dominguez-Rodriguez, D.-S. Cheong, and A. H. Heuer, Philos. Mag. A **60**, 107 (1989).
[4] D.-S. Cheong, A. Dominguez-Rodriguez, and A. H. Heuer, Philos. Mag. A **60**, 123 (1989).
[5] D.-S. Cheong, A. Dominguez-Rodriguez, and A. H. Heuer, Philos. Mag. A **63**, 377 (1991).
[6] A. Dominguez-Rodriguez, D.-S. Cheong, and A. H. Heuer, Philos. Mag. A **64**, 923 (1991).
[7] J. Martinez-Fernandez, M. Jimenez-Melendo, A. Dominguez-Rodriguez, and A. H. Heuer, J. Am. Ceram. Soc. **73**, 2452 (1990).
[8] D. Goméz-Garcia, J. Martinez-Fernandez, A. Dominguez-Rodriguez, P. Eveno, and J. Castaing, Acta Mater. **44**, 991 (1996).
[9] D. Goméz-Garcia, J. Martinez-Fernandez, A. Dominguez-Rodriguez, and J. Castaing, J. Am. Ceram. Soc. **80**, 1668 (1997).
[10] K. J. McClellan, A. H. Heuer, and L. Kubin, Acta Mater. **44**, 2651 (1996).
[11] U. Messerschmidt, B. Baufeld, K. J. McClellan, and A. H. Heuer, Acta Metall. Mater. **43**, 1917 (1995).
[12] F. R. Chien and A. H. Heuer, Philos. Mag. A **73**, 2733 (1996).
[13] B. Baufeld, D. Baither, M. Bartsch, and U. Messerschmidt, phys. stat. sol. (a) **166**, 127 (1998).
[14] B. Burton, Mater. Sci. Technol. **5**, 1005 (1989).
[15] T. A. Parthasarathy and R. S. Hay, Acta Mater. **44**, 4663 (1996).
[16] B. Baufeld, M. Bartsch, U. Messerschmidt, and D. Baither, Acta Metall. Mater. **43**, 1925 (1995).
[17] B. Baufeld, B. V. Petukhov, M. Bartsch, and U. Messerschmidt, Acta Metall. Mater. **46**, 3077 (1998).
[18] P. Teracher, H. Garem, and J. Rabier, in: Strength of Metals and Alloys, edited by D. G. Brandon, R. Chaim, and A. Rosen. Freund Publs. (London, 1991) p. 217.
[19] B. V. Petukhov, M. Bartsch, and U. Messerschmidt, Eur. Phys. J. Applied Phys. **9**, 89 (2000).
[20] U. Messerschmidt, B. Baufeld, and D. Baither, Key Eng. Mater. **153–154**, 143 (1998).
[21] U. Messerschmidt, D. Baither, B. Baufeld, and M. Bartsch, Mater. Sci. Eng. A **233**, 61 (1997).
[22] D. Baither, B. Baufeld, U. Messerschmidt, and M. Bartsch, Mater. Sci. Eng. A **233**, 75 (1997).
[23] A. Dominguez-Rodriguez and A. H. Heuer, Cryst. Lattice Defects Amorph. Mat. **16**, 117 (1987).
[24] G. Schöck, phys. stat. sol. (a) **8**, 499 (1965).
[25] B. Baufeld, Doctoral thesis (Martin-Luther-Universität, Halle/Wittenberg, 1996).
[26] P. J. Botha, J. C. H. Chiang, J. D. Comins, P. M. Mjwara, and P. E. Ngoepe, J. Appl. Phys. **73**, 7268 (1993).
[27] G. J. Taylor, Proc. Roy. Soc. **A 145**, 362 (1934).
[28] M. Weller, Z. Metallkunde **84**, 6 (1993).
[29] M. Weller and A. Lakki, Ber. Bunsenges. Phys. Chem. **101**, 1297 (1997).
[30] A. Lakki, R. Herzog, M. Weller, H. Schubert, C. Reetz, O. Görke, M. Kilo, and G. Borchardt, J. Europ. Ceram. Soc. **20**, 285 (2000).
[31] M. Weller and H. Schubert, J. Am. Ceram. Soc. **69**, 573 (1986).
[32] H. Solman, J. Chaumont, C. Dolin, and C. Monty, Ceram. Trans. **24**, 175 (1991).
[33] D. Gomez-Garcia, J. Martinez-Fernandes, A. Dominguez-Rodriguez, and K. H. Westmacott, Phil. Mag. A **79**, 1839 (1999).
[34] G. van Tendeloo, L. Anders, and G. Thomas, Acta Metall. **31**, 1619 (1983).
[35] A. Portevin and F. Le Chatelier, Comp. Rend. Sci. Paris **176**, 507 (1923).
[36] W. R. Cannon and T. G. Langdon, J. Mater. Sci. **18**, 1 (1983).
[37] U. F. Kocks, J. Eng. Mater. Technol. **98**, 76 (1976).
[38] U. F. Kocks, Physical Basis for Non-Elastic Constitutive Relations, Discussion paper at Symp. Adv. in Metal Deformation, Cornell Univ. (Ithaca NY, 1976).
[39] Y. Oishi, K. Ando, and Y. Sakka, in Advances in Ceramics, edited by M. F. Yang and A. H. Heuer, Vol. 7. Am. Ceram. Soc. (Westerville OH, 1989), p. 208.
[40] M. Kilo, G. Borchardt, S. Weber, S. Scherrer, and K. Tinschert, Ber. Bunsenges. Phys. Chem. **101**, 1361 (1997).
[41] A. Dominguez-Rodriguez, A. H. Heuer, and J. Castaing, Rad. Eff. Diff. Solids **119–121**, 759 (1991).